

Bimetallic PCN-333 with Modulated Crystallization and a Porosity Structure for a Highly Efficient Removal of Congo Red

Boxi Li, Xufeng Zhang,* Jing Shen,* Aihua Zhang, and He Huang

Cite This: *ACS Omega* 2024, 9, 7173–7187

Read Online

ACCESS |



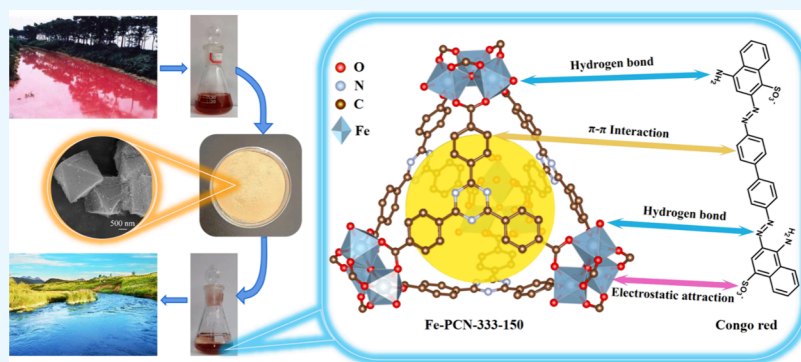
Metrics & More



Article Recommendations



Supporting Information



ABSTRACT: Bimetallic metal–organic frameworks (BMOFs) have garnered significant attention in the field of environmental remediation due to their more diverse adsorption sites compared to monometallic metal–organic frameworks (MOFs). Different energy barriers must be overcome for different metal ions and organic linkers to form MOFs. However, the impact of the synthesis temperature on the crystallization and porosity structure of BMOFs has been rarely studied. In this work, PCN-333 series-based BMOFs with different Fe/Al ratios were prepared by a solvothermal method at temperatures of both 135 and 150 °C. The synthesis temperature and Fe/Al ratio have significant effects on the crystal structure and specific surface area of bimetallic PCN-333, leading to the different adsorption performance of the PCN-333 for Congo red (CR). The Fe/Al-PCN-333–135(3:1) and Fe-PCN-333–150 exhibited the maximum CR adsorption capacities of 3233 and 3933 mg/g, respectively, surpassing the capacities of most previously documented adsorbents. The Langmuir model and pseudo-second-order kinetics can well describe the adsorption process of CR on Fe/Al-PCN-333–135(3:1) and Fe-PCN-333–150. Combining the isotherm adsorption behavior with the thermodynamic parameters, CR adsorption on BMOFs is a single-layer endothermic chemical adsorption. Furthermore, Fe/Al-PCN-333–135(3:1) and Fe-PCN-333–150 exhibited regenerability and reusability for three cycles with reasonable efficiency. This work is of great significance in the field of engineering BMOF materials to treat dye wastewater.

1. INTRODUCTION

The global issue of water pollution stemming from organic dyes has emerged as a significant environmental concern.^{1,2} As industrialization progresses, various organic dyes are widely used in printing, plastics, textile, rubber, and other industries, resulting in hundreds of thousands of tons of dye waste every year.³ These dyes contain harmful aromatic structures that are highly carcinogenic and are difficult to biodegrade, posing a threat to human health and ecological safety. Congo red (CR) is a widely used anionic azo dye with nonbiodegradable properties and high biological toxicity, which can cause reproductive disorders and even cancer to humans.⁴ Therefore, it is necessary to exploit efficient strategies for the removal of CR from wastewater. Currently, prominent techniques for treating dye-contaminated wastewater encompass chemical precipitation,⁵ oxidation,⁶ photocatalytic degradation,⁷ coagulation/flocculation,⁸ membrane separation,⁹ reverse osmosis,¹⁰ and adsorption.¹¹ Among these methods, adsorption stands

out due to its straightforward operation, high efficiency, and absence of secondary pollution.¹² Traditional dye adsorbents include activated carbon,¹³ cellulose,¹⁴ zeolite,¹⁵ chitosan,¹⁶ graphene oxide,¹⁷ and so on. However, their adsorption capacity for numerous dyes is relatively low. Therefore, there is an urgent and imperative need to develop adsorbents with a high adsorption efficiency for organic dyes.

In recent years, metal–organic frameworks (MOFs) have attracted widespread attention as an emerging class of materials.¹⁸ MOFs are characterized as porous crystalline

Received: November 20, 2023

Revised: January 5, 2024

Accepted: January 9, 2024

Published: January 30, 2024



materials formed by the self-assembly of metal ions or metal clusters and organic linkers.¹⁹ Due to their advantages such as high porosity, a high specific surface area, and a large number of unsaturated metal sites, MOFs have attracted increasing attention in the realm of wastewater treatment.^{20–23} In addition, under different synthesis conditions such as the temperature and reactant ratio, the crystal structure and surface morphology of MOFs change,^{24–26} thereby exerting a significant impact on their adsorption performance. For instance, when the size of the MOF particles is large or the coordination binding energy between the metal nodes and the organic linkers is too strong, the target molecules will be prevented from entering the MOF framework or binding to the adsorption site of MOFs.²⁷ Therefore, regulating the crystallization and morphology of MOFs to improve their adsorption performance is of great significance for the treatment of dye-contaminated wastewater. Currently, researchers tend to combine two or more metal ions to form bimetallic or multimetallic MOF materials, hoping to increase the specific surface area by reducing the particle size of the MOF, or combine the advantages of various components to obtain some special properties.^{28,29} Yang et al. successfully prepared Fe-ZIF-8–500 by using iron ions as a modulator.³⁰ Since the doped Fe ions provided additional adsorption sites, the adsorption capacity of the optimized Fe-ZIF-8–500 for tetracycline reached 867 mg/g, which was significantly higher than the 214 mg/g of the original ZIF-8. Liu et al.³¹ adjusted the morphology and size of HKUST-1 by adding inorganic salts. They found that Na⁺ could interact with the organic linker to reduce the crystal nucleation rate, successfully preparing MOFs with different morphologies and sizes.³¹ Gu et al. successfully prepared a series of MOFs with different particle sizes and specific surface areas by adjusting the ratio of Fe and Mg ions.³² Fe/Mg-MIL-88B had a higher arsenate absorption capacity compared with the monometallic Fe-MIL-88B. Additionally, the reaction temperature also plays an important role in solvothermal synthesis of MOFs. The production of MOFs, like other reactions, requires energy extraction at a certain temperature to overcome the energy barrier.³³ Jiang et al. prepared Co-MOF-74 at different temperatures.³⁴ Co-MOF-74 synthesized at 100 °C exhibited a flowerlike morphology, while others exhibited a hexagonal prism morphology. Co-MOF-74–100 °C had the largest specific surface area and pore volume, reaching 928.9 m²/g and 0.4296 cm³/g, respectively. However, there are few works in the literature that simultaneously explore the adjustment of synthesis temperature and bimetal ratio on the MOF structure, thereby affecting the adsorption properties.

PCN-333 is a water-stable MOF that is characterized by its exceptionally high specific surface area and pore volume. The formation of PCN-333 entails the autonomous assembly of metal clusters and organic ligands into a microporous tetrahedral cage. Subsequently, the metal clusters within these tetrahedral cages are shared, resulting in the formation of larger mesoporous cages.^{35,36} The structural diagram of PCN-333 can be observed in Figure S1. The large specific surface area and cage structure of PCN-333 facilitate enhanced the contact and capture of adsorbed materials by the MOF. In this work, PCN-333 series-based BMOFs with different Fe/Al ratios was prepared at two temperatures of 135 and 150 °C. The two temperatures were chosen because Fe-PCN-333 was reported to be synthesized at 150 °C, whereas Al-PCN-333 is synthesized at 135 °C.³⁶ Higher synthesis temperatures

indicate that the coordination bonding energy barrier between Fe and the organic linker of H₃TATB (4,4',4''-s-triazine-2,4,6-triyl-tribenzoic acid) is higher than that between Al and H₃TATB. The novelty of our work is that we studied for the first time the effect of the synthesis temperature on the crystallization of the BMOFs with different coordination energy barriers between metal ions and organic linkers. The molar ratio of Fe to Al ions and the synthesis temperature affect the final morphology and microstructural features of the material, helping to optimize the adsorption performance of the material for CR. The effects of the initial pH, adsorption time, and initial concentration on CR adsorption performance were explored. The possible adsorption mechanism was analyzed using X-ray photoelectron spectroscopy (XPS) and Fourier transform infrared spectroscopy (FT-IR). Since the reuse of adsorbents is important from both practical application and economic perspectives, we investigated the regeneration and reusability of the best performing BMOFs of Fe-PCN-333–150 and Fe/Al-PCN-333–135(3:1). The results show that Fe-PCN-333–150 and Fe/Al-PCN-333–135(3:1) have great potential to remove CR from wastewater.

2. MATERIALS AND METHODS

2.1. Materials. 4,4',4''-s-Triazine-2,4,6-triyl-tribenzoic acid (H₃TATB, 97% purity) and trifluoroacetic acid (99% purity) were purchased from Shanghai Macklin Biochemical Co., Ltd. Aluminum chloride hexahydrate (AlCl₃·6H₂O, AR grade), ferric chloride (FeCl₃, AR grade), Congo red (CR), *N,N*-dimethylformamide (DMF, ≥ 99.5% purity), and acetone (≥99.5% purity) was obtained from Tianjin Concord Technology Co., Ltd. All chemicals were of analytical grade and can be used directly without further treatment. Deionized (DI) water was used throughout the experiments.

2.2. Preparation of Adsorbents. **2.2.1. Synthesis of Al-PCN-333–135 and Fe-PCN-333–150.** Al-PCN-333–135 or Fe-PCN-333–150 was synthesized according to recently published articles with slight modifications.³⁶

Synthesis of Al-PCN-333–135. H₃TATB (50 mg, 0.113 mmol) and AlCl₃·6H₂O (200 mg, 0.828 mmol) were dissolved in 10 mL of DMF, and then 1.0 mL of trifluoroacetic acid was added. The mixture was heated in an oven at 135 °C for two days until a white precipitate formed. The white precipitate was centrifuged and washed successively with fresh DMF and acetone for several times. The acetone-exchanged Al-PCN-333–135 was dried at 85 °C for 1 h.

Synthesis of Fe-PCN-333–150. H₃TATB (50 mg, 0.113 mmol) and FeCl₃ (60 mg, 0.370 mmol) were dissolved in 10 mL of DMF, and then 0.5 mL of trifluoroacetic acid was added. The mixture was heated in an oven at 150 °C for 12 h until a brown precipitate formed. The brown precipitate was centrifuged and washed successively with fresh DMF and acetone for several times. The acetone-exchanged Fe-PCN-333–150 was dried at 85 °C for 1 h.

2.2.2. Synthesis of Fe/Al-PCN-333–135. H₃TATB (50 mg, 0.113 mmol) and a certain amount of AlCl₃·6H₂O (0.621, 0.414, 0.207, and 0 mmol) and FeCl₃ (0.207, 0.414, 0.621, and 0.828 mmol) are dissolved in 10 mL of DMF then 1.0 mL of trifluoroacetic acid was added. The mixture was heated in an oven at 135 °C for two days. The molar ratios of Fe to Al in precursor solution were 1:3 (Fe/Al-PCN-333–135(1:3)), 1:1 (Fe/Al-PCN-333–135(1:1)), 3:1 (Fe/Al-PCN-333–135(3:1)), and 1 (Fe-PCN-333–135). The precipitates were

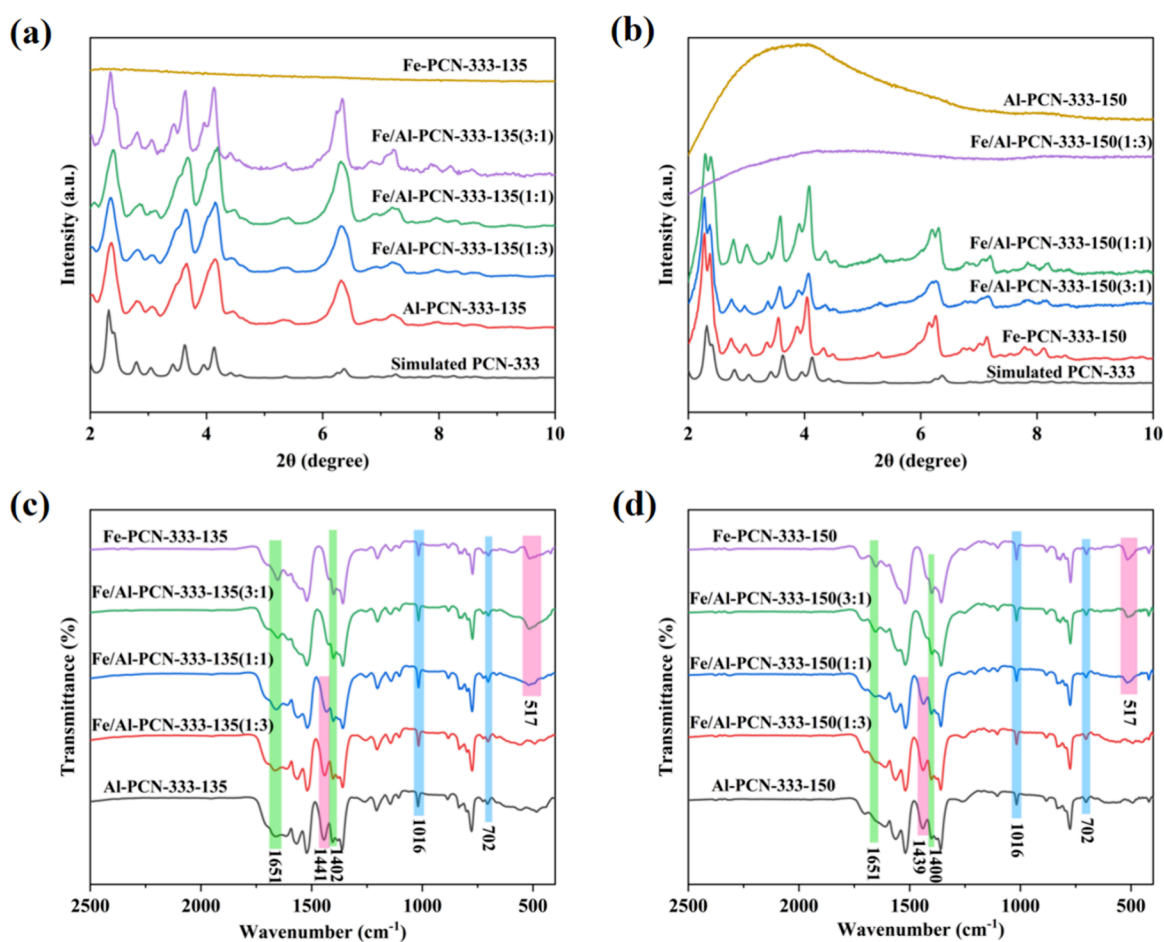


Figure 1. PXRD spectra of (a) PCN-333–135 and (b) PCN-333–150 series samples; FT-IR spectra of (c) PCN-333–135 and (d) PCN-333–150 series samples.

centrifuged, washed successively with fresh DMF and acetone several times, and dried at 85 °C for 1 h for use.

2.2.3. Synthesis of Fe/Al-PCN-333–150. H₃TATB (50 mg, 0.113 mmol) and a certain amount of AlCl₃·6H₂O (0.0925, 0.185, 0.2775, and 0.370 mmol) and FeCl₃ (0.2775, 0.185, 0.0925, and 0 mmol) are dissolved in 10 mL of DMF, and then 0.5 mL of trifluoroacetic acid was added. The mixture was heated in an oven at 150 °C for 12 h. The molar ratios of Fe to Al in precursor solution were 1:3 (Fe/Al-PCN-333–150(1:3)), 1:1 (Fe/Al-PCN-333–150(1:1)), 3:1 (Fe/Al-PCN-333–150(3:1)), and 1 (Al-PCN-333–150). The precipitates were centrifuged, washed successively with fresh DMF and acetone several times, and dried at 85 °C for 1 h for use.

2.3. Characterizations. The physicochemical properties of the as-synthesized BMOFs were characterized by the powder X-ray diffraction (PXRD), scanning electron microscope (SEM), X-ray photoelectron spectra (XPS), thermogravimetric analyses (TGA), Fourier transform infrared spectra (FT-IR), and Brunauer–Emmett–Teller (BET).

2.4. Adsorption Experiments. In all of the adsorption experiments, CR solutions were prepared using CR and deionized water. Unless otherwise stated, batch adsorption experiments were performed on a constant-temperature shaker with an aqueous solution volume of 30 mL, a temperature of 298 K, a stirring speed of 120 rpm, and 5 mg of the adsorbent. In the kinetic experiment, the CR concentration was 400 mg/L with the contact time ranging from 5 to 360 min. The isotherm

experiment was carried out at 298 K, and the initial concentrations of CR solution ranged from 100 to 1000 mg/L. Thermodynamic experiments were conducted at 298, 308, and 318 K with an initial CR concentration of 1000 mg/L. To investigate the effect of different dosages on CR adsorption performance, 2.5–12.5 mg of the adsorbent was added to 30 mL of CR solution with an initial concentration of 500 mg/L. To explore the influence of the pH value on adsorption performance, the pH value of CR solutions was adjusted by adding 0.1 mol/L HCl or NaOH.

The CR concentration was measured at 496 nm using a UV–vis spectrometer. The standard curve of CR is shown in Figure S2. The adsorption capacity was calculated as follows:

$$q_t = \frac{(c_0 - c_t) \times V}{m} \quad (1)$$

$$q_e = \frac{(c_0 - c_e) \times V}{m} \quad (2)$$

where c_0 (mg/L), c_t (mg/L), and c_e (mg/L) are the initial, t time, and equilibrium concentrations of CR solution, respectively, q_t (mg/g) and q_e (mg/g) are the adsorption capacities at t time and equilibrium, respectively, V (L) is the volume of the CR solution, and m (g) is the mass of the adsorbent. All experiments were repeated at least three times.

The removal efficiency (R , %) was calculated as follows:

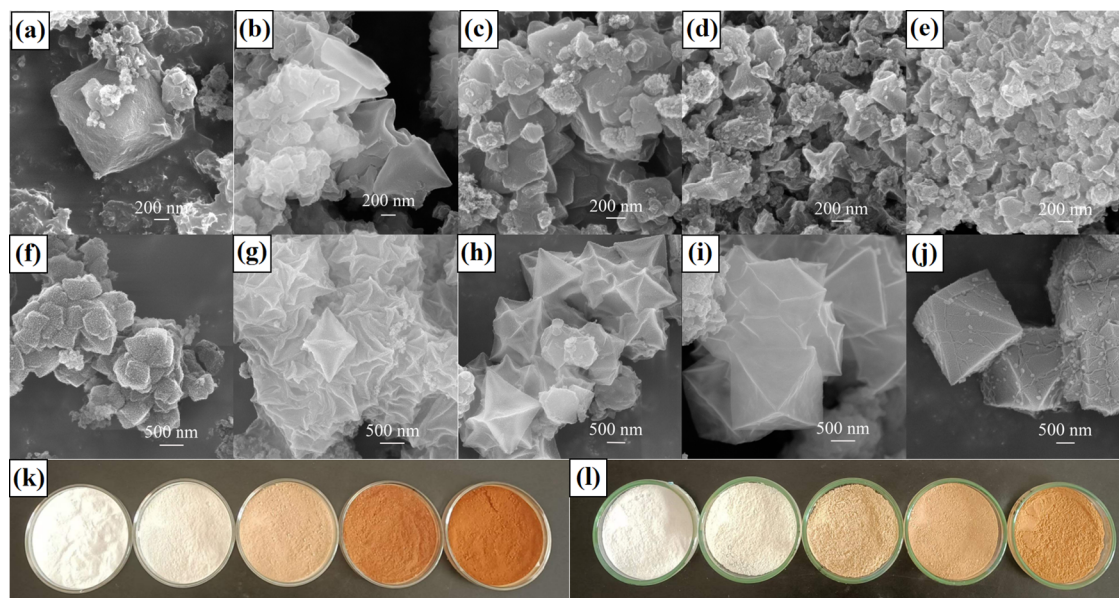


Figure 2. SEM images of (a) Al-PCN-333–135, (b) Fe/Al-PCN-333–135(1:3), (c) Fe/Al-PCN-333–135(1:1), (d) Fe/Al-PCN-333–135(3:1), (e) Fe-PCN-333–135, (f) Al-PCN-333–150, (g) Fe/Al-PCN-333–150(1:3), (h) Fe/Al-PCN-333–150(1:1), (i) Fe/Al-PCN-333–150(3:1), and (j) Fe-PCN-333–150 and macroscopic photographs of (k) PCN-333–135 series samples and (l) PCN-333–150 series samples with the increase of the Fe amount.

$$R = \frac{c_0 - c_e}{c_0} \times 100 \quad (3)$$

To explore the reusability of the adsorbent, 10 mg of the adsorbent was added to 60 mL of CR solution (400 mg/L, pH 5). After the adsorption equilibrium was reached, the adsorbent-loaded CR was shaken with 60 mL of the eluent at 120 rpm and 298 K for a specific time to determine the concentration of CR in the eluent. The adsorbent loaded CR was washed several times with the eluent until no CR was present in the eluent, and the regenerated adsorbent was dried in an oven at 85 °C for subsequent use. The desorption quantity (q_d , mg/g) and desorption efficiency (D , %) were calculated as follows

$$q_d = \frac{c_{\text{eluent}} \times V_{\text{eluent}}}{m} \quad (4)$$

$$D = \frac{q_d}{q_e} \times 100 \quad (5)$$

where c_{eluent} (mg/L) and V_{eluent} (L) refer to the CR concentration and volume of the eluent after desorption, respectively.

3. RESULTS AND DISCUSSION

3.1. Morphology and Structural Characterization.

3.1.1. PXRD and FT-IR Analysis. The crystallization behavior of the prepared MOF materials was analyzed by PXRD. As shown in Figure 1a,b, the main diffraction peaks of most of the prepared adsorbents are in good agreement with the simulated pattern from the crystallographic information file.³⁶ As the additional amount of FeCl₃ or AlCl₃·6H₂O increases, only the intensities of several characteristic peaks change, which implies that the PCN-333–135 and PCN-333–150 series samples were successfully prepared. The crystallinity of each product was determined by analyzing the XRD pattern, and the result is presented in Table S1. It is evident that the crystallinity of the

product exhibits a gradual decline as the FeCl₃ content increases at a temperature of 135 °C. Similarly, at a temperature of 150 °C, the crystallinity of the product gradually diminishes with an increase in the AlCl₃·6H₂O content. The PXRD spectra of Fe-PCN-333–135, Al-PCN-333–150, and Fe/Al-PCN-333–150(1:3) exhibited an absence of distinct diffraction peaks, suggesting the absence of crystallization in these three samples. This unanticipated outcome could potentially be attributed to the mismatch in the synthesis temperature and coordination binding energy between the metal ions and organic linkers.

To explore the characteristic functional groups of the prepared PCN-333 materials, FT-IR spectra are shown in Figure 1c,d. The –COOH vibration peaks at 1651 and 1402/1400 cm^{−1} confirmed the existence of dicarboxylate coordinated with metal ions.³⁷ The peaks at 1016 cm^{−1} (C=C) and 702 cm^{−1} (C=N) are the characteristic peaks of aromatic heterocycles and triazine nuclei, illustrating the existence of the H₃TATB linker.³⁸ In addition, the peaks at 1441/1439 and 517 cm^{−1} represent the stretching modes of Al–O and Fe–O, respectively.

3.1.2. SEM Analysis. The electron microscopy and macroscopic photographs of the PCN-333 synthesized with different Fe/Al ratios at 135 and 150 °C are shown in Figure 2. As depicted in Figure 2a,j, the monometallic PCN-333 of Al-PCN-333–135 and Fe-PCN-333–150 exhibits an octahedral crystal morphology with average crystal diameters of 1.3 and 2.5 μm, respectively. However, the addition of secondary metal ions resulted in the reduction of the octahedral crystals and the increase of lamellar agglomerates, as depicted in Figure 2b–i. This result is consistent with the PXRD spectra of the PCN-333 series samples. Moreover, the particle size gradually decreased with the addition of secondary metal ions. As shown in Figure 2b–e and Figure S3, the particle sizes of PCN-333–135 series samples gradually decrease with the increasing amount of FeCl₃. The particle size of Fe/Al-PCN-333–135(1:3), Fe/Al-PCN-333–135(1:1), Fe/Al-PCN-333–

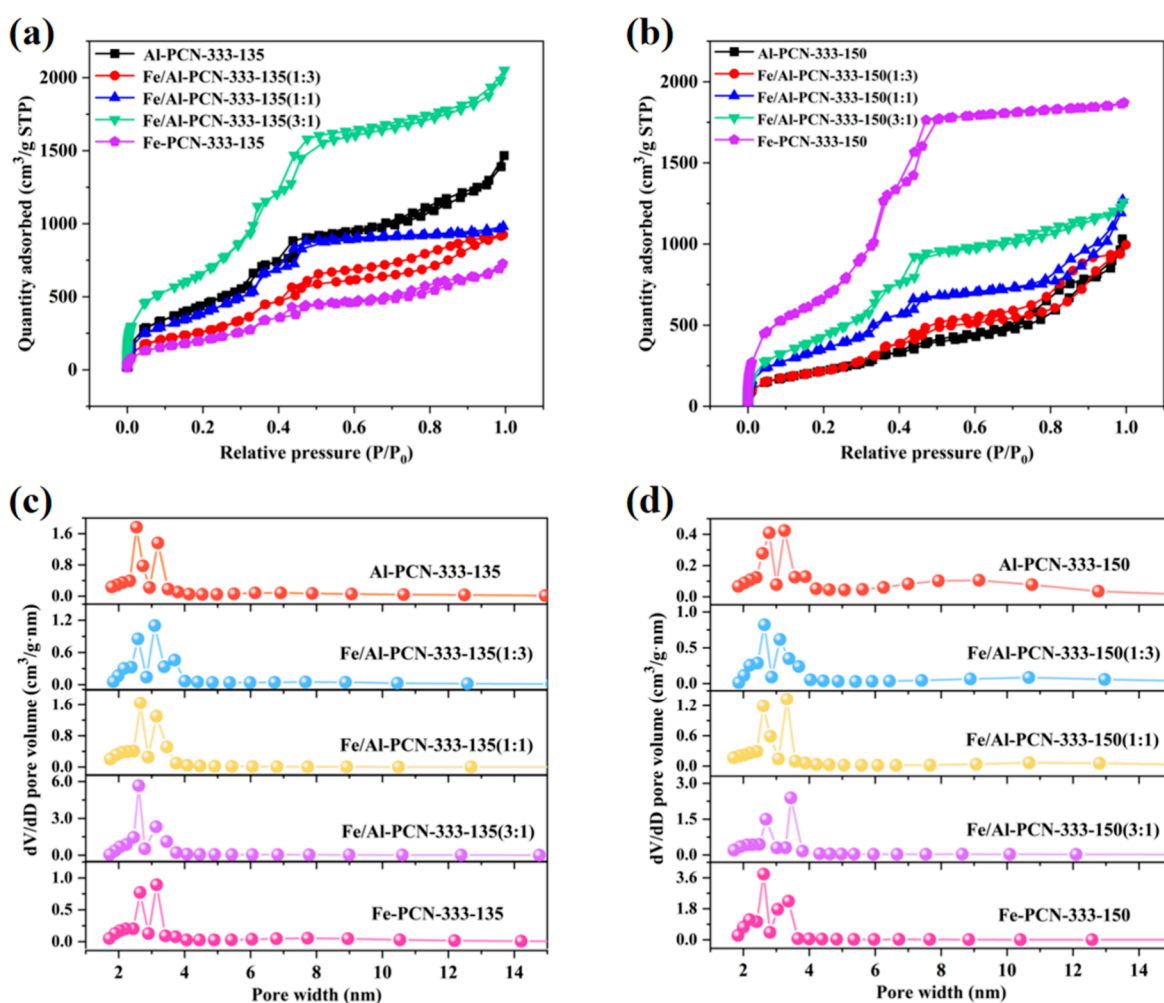


Figure 3. N_2 adsorption–desorption isotherms of (a) PCN-333–135 and (b) PCN-333–150 series samples; pore size distribution curves of (c) PCN-333–135 and (d) PCN-333–150 series samples.

135(3:1), and Fe-PCN-333–135 was measured to be 1.13, 0.75, 0.60, and 0.53 μm , respectively. Likewise, as depicted in Figure 2f–i and Figure S4, the particle sizes of PCN-333–150 series samples gradually decreased with the increasing amount of $\text{AlCl}_3 \cdot 6\text{H}_2\text{O}$. The particle sizes of Fe/Al-PCN-333–150(3:1), Fe/Al-PCN-333–150(1:1), Fe/Al-PCN-333–150(1:3), and Al-PCN-333–150 were measured to be 1.87, 1.67, 1.04, and 0.62 μm , respectively.

3.1.3. BET Analyses. The specific surface area and pore size of the PCN-333–135 and PCN-333–150 series samples were determined by N_2 adsorption–desorption experiments. The results are shown in Figure 3a–d and Tables S2 and S3. In the extremely low-pressure range ($P/P_0 < 0.05$), all the materials exhibited rapid N_2 absorption, indicating the presence of micropores. Moreover, a hysteresis loop appears in the relative pressure range of 0.4–1.0 P/P_0 for all samples, indicating the existence of mesopores. Significantly, the specific surface area of bimetallic PCN-333 was greatly affected by the Fe/Al ratio and the synthesis temperature. For the PCN-333–135 series samples prepared at 135 $^\circ\text{C}$, the specific surface area of Fe/Al-PCN-333–135(3:1) was much higher than that of other PCN-333–135 samples. For the PCN-333–150 series samples prepared at 150 $^\circ\text{C}$, the specific surface area of Fe-PCN-333–150 was much higher than that of other PCN-333–150 samples. Both Fe/Al-PCN-333–135(3:1) and Fe-PCN-333–

150 exhibit remarkably high specific surface areas as evidenced by the pore size distribution curves depicted in Figure 3c,d. Notably, when compared to other series samples, these two samples demonstrate a substantial increase in pore volume within the 2–4 nm pore size range, indicating the presence of hierarchical porosity.³⁹ This increase in the pore volume is advantageous for enhancing the specific surface area and facilitating the exposure of additional active sites.^{40,41}

3.1.4. Thermogravimetric and XPS Analysis. Thermogravimetric analysis (TGA) curves can reflect the thermal stability of bimetallic PCN-333 samples, as shown in Figure 4a,b. All of the TGA curves show two main mass loss regions. The first mass loss is mainly caused by the evaporation of acetone and DMF solvent, and the second mass loss is caused by decomposition of the framework. For the PCN-333–135 series of samples, the decomposition temperature of monometallic Al-PCN-333–135 was 500 $^\circ\text{C}$, which is significantly higher than that of monometallic Fe-PCN-333–135 of 360 $^\circ\text{C}$. Meanwhile, the decomposition temperature of all bimetallic Fe/Al-PCN-333–135 samples was between monometallic Al-PCN-333–135 and Fe-PCN-333–135. This result indicated that the thermal stability of Al-PCN-333 is higher than that of Fe-PCN-333. Likewise, the decomposition temperature of 510 $^\circ\text{C}$ for monometallic Al-PCN-333–150 is significantly higher than 400 $^\circ\text{C}$ for monometallic Fe-PCN-

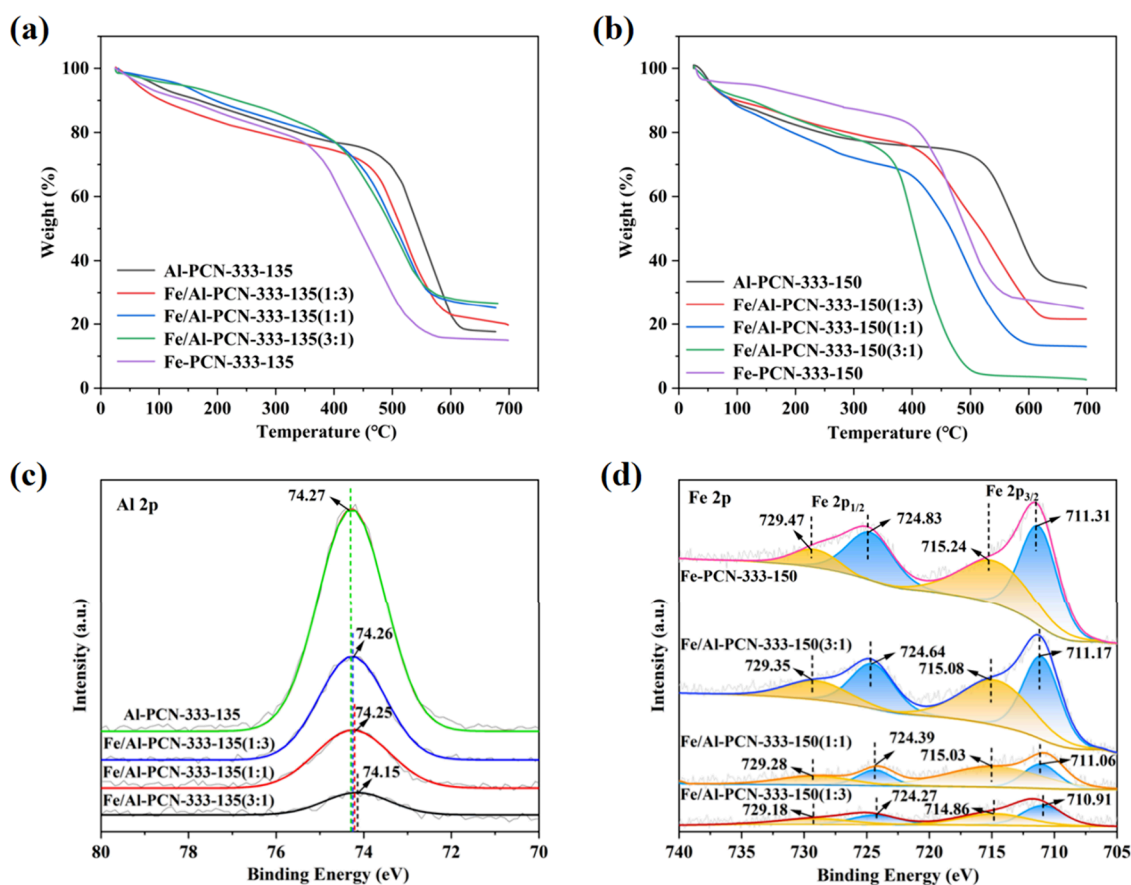


Figure 4. TGA curves of (a) the PCN-333–135 series samples and (b) the PCN-333–150 series samples. XPS spectra of (c) Al 2p for PCN-333–135 series samples and (d) Fe 2p for PCN-333–150 series samples.

333–150. It is noteworthy that the decomposition temperatures of PCN-333–150 series samples are higher than that of corresponding PCN-333–135 series samples. The results show that the higher synthesis temperature of 150 °C contributes to improve the thermal stability of Fe/Al-PCN-333.

XPS was used to further understand the crystal defects of PCN-333–135 and PCN-333–150, and the results are shown in Figure 4c,d. By comparing the coordination number changes of Fe or Al, the defects can be determined indirectly.³⁹ For the PCN-333–135 series samples, the binding energy of Al 2p gradually decreased with the Fe increase, indicating that the coordination number of Al decreased and the defect content gradually increased. For the PCN-333–150 series samples, as the Al content increases, the binding energy of Fe 2p gradually moved to a lower level, indicating that the coordination number of Fe decreased and the defect content gradually increased. Defects can lead to the exposure of additional unsaturated coordination sites,⁴² which may enhance the CR adsorption capacity of the PCN-333.

3.2. Adsorption Performance. **3.2.1. Effect of Fe/Al Ratios.** To investigate the effect of the Fe/Al ratio of bimetallic PCN-333 on the CR adsorption performance, PCN-333–135 and PCN-333–150 samples with different Fe/Al ratios were used to determine their CR adsorption capacities at different initial CR concentrations. As shown in Figure 5a,b, the adsorption capacities of all the adsorbents were enhanced with the increase of the initial CR concentration. For the PCN-333–135 series samples, the adsorption capacity of Fe/Al-PCN-333–135(3:1) is superior to other adsorbents. However,

for the PCN-333–150 series samples, Fe-PCN-333–150 has the highest adsorption capacity. The high adsorption capacity may be attributed to their elevated specific surface areas, as evidenced by the data presented in Tables S2 and S3. Consequently, Fe/Al-PCN-333–135(3:1) and Fe-PCN-333–150 are chosen for further investigation in subsequent research endeavors.

3.2.2. Effects of Dosages. Figure 5c,d shows the effects of the dosage of Fe/Al-PCN-333–135(3:1) and Fe-PCN-333–150 on the CR adsorption capacity and removal efficiency. As the dosage of the two BMOFs increased, the removal efficiency increased and the adsorption capacity declined. When the dosage increased from 0.083 mg/mL to 0.417 mg/mL, the CR removal efficiency of Fe/Al-PCN-333–135(3:1) and Fe-PCN-333–150 increased from 53.2 to 92.1% and from 55.8 to 97.6%, respectively. Meanwhile, the adsorption capacity of Fe/Al-PCN-333–135(3:1) and Fe-PCN-333–150 decreased from 3190.2 to 1104.9 mg/g and from 3346.5 to 1171.1 mg/g, respectively. When the dosage of the adsorbent was higher than 0.167 mg/mL, the CR removal efficiency gradually stabilized. The initial significant increase in CR removal efficiency is due to the increase in CR binding active sites. However, overuse of adsorbents can result in redundant active sites, leading to unsaturated adsorption and low adsorption capacity, thus hindering the full utilization of adsorbents. Therefore, we selected the dosage of Fe/Al-PCN-333–135(3:1) and Fe-PCN-333–150 to be 0.167 mg/mL for further study.

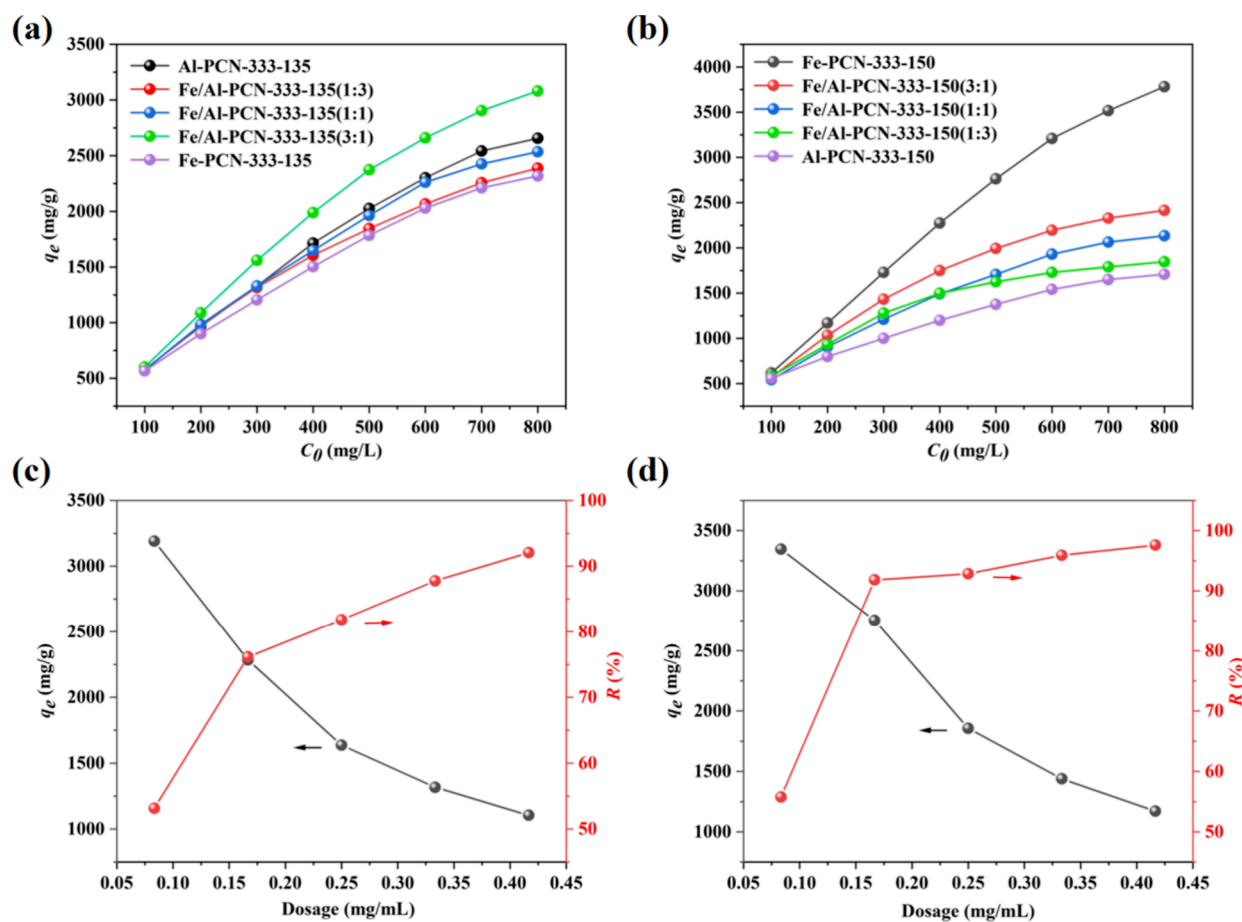


Figure 5. Adsorption capacity of (a) PCN-333-135 and (b) PCN-333-150 samples in different initial concentrations of CR solution with a dosage of 0.167 mg/mL. To ensure the adsorption equilibrium, the contact time was set for 6 h. Effect of the dosages of (c) Fe/Al-PCN-333-135(3:1) and (d) Fe-PCN-333-150 on CR adsorption performance with an initial CR concentration of 500 mg/mL.

3.2.3. Influence of the Initial pH. pH value is one of the key factors affecting adsorption properties, which changes the surface charge of the adsorbent and CR molecules. Figure 6a shows the effect of the pH value on the CR adsorption capacity of Fe/Al-PCN-333-135(3:1) and Fe-PCN-333-150. It was found that as the pH value increases from 3 to 5, the adsorption capacities of Fe/Al-PCN-333-135(3:1) and Fe-PCN-333-150 gradually increase and reach the maximum value of 2283.7 and 2754.6 mg/g, respectively. With the further increase of the pH value, the adsorption capacity of the two adsorbents gradually decreased. CR is an anionic azo dye. Its sulfonate moiety contains a negative sulfonic acid group, and its isoelectric point is approximately 3.¹ Therefore, the surface charge of the CR in our experiment is negative. In addition, the metal ions of Fe/Al-PCN-333-135(3:1) and Fe-PCN-333-150 exhibit a positive charge under acidic conditions. Therefore, under acidic conditions, the positively charged adsorbent generates a strong electrostatic attraction with the negatively charged CR, resulting in higher adsorption capacity. With the increase of the alkalinity of the solution, the positive charge on the adsorbent surface declines, so the adsorption capacities gradually decrease. On the other hand, large numbers of OH⁻ in alkaline solution compete with CR molecules for adsorption sites, resulting in the reduction of adsorption capacity. Therefore, the optimal pH value for CR adsorption by Fe/Al-PCN-333-135(3:1) and Fe-PCN-333-150 was obtained to be 5.

3.2.4. Adsorption Kinetics. To reveal the mass transfer mechanism and rate-limiting steps of the adsorption process, pseudo-first-order, pseudo-second-order, and Weber-Morris intraparticle diffusion models were used to simulate the adsorption kinetics of Fe/Al-PCN-333-135(3:1) and Fe-PCN-333-150 on CR. The equations of the three kinetic models are shown as follows

$$\text{Pseudo-first-order: } \ln(q_e - q_t) = \ln q_e - k_1 t \quad (6)$$

$$\text{Pseudo-second-order: } \frac{t}{q_t} = \frac{1}{k_2 q_e^2} + \frac{t}{q_e} \quad (7)$$

$$\text{Weber-Morris intraparticle diffusion: } q_t = k_{id} t^{0.5} + C \quad (8)$$

where k_1 (min⁻¹), k_2 (mg⁻¹·g·min⁻¹), and k_{id} (mg·g⁻¹·min^{-0.5}) are the rate constants of the pseudo-first-order, pseudo-second-order, and Weber-Morris intraparticle diffusion models, respectively.

The influence of the contact time on the adsorption behaviors is presented in Figure 6b. In the initial 30 min, Fe/Al-PCN-333-135(3:1) and Fe-PCN-333-150 showed a rapid adsorption rate and gradually reached equilibrium within 240 min. Moreover, Fe-PCN-333-150 has a higher adsorption capacity and faster CR adsorption rate than Fe/Al-PCN-333-135(3:1), which may be due to the larger specific surface area of Fe-PCN-333-150. The linear fittings of the pseudo-first-

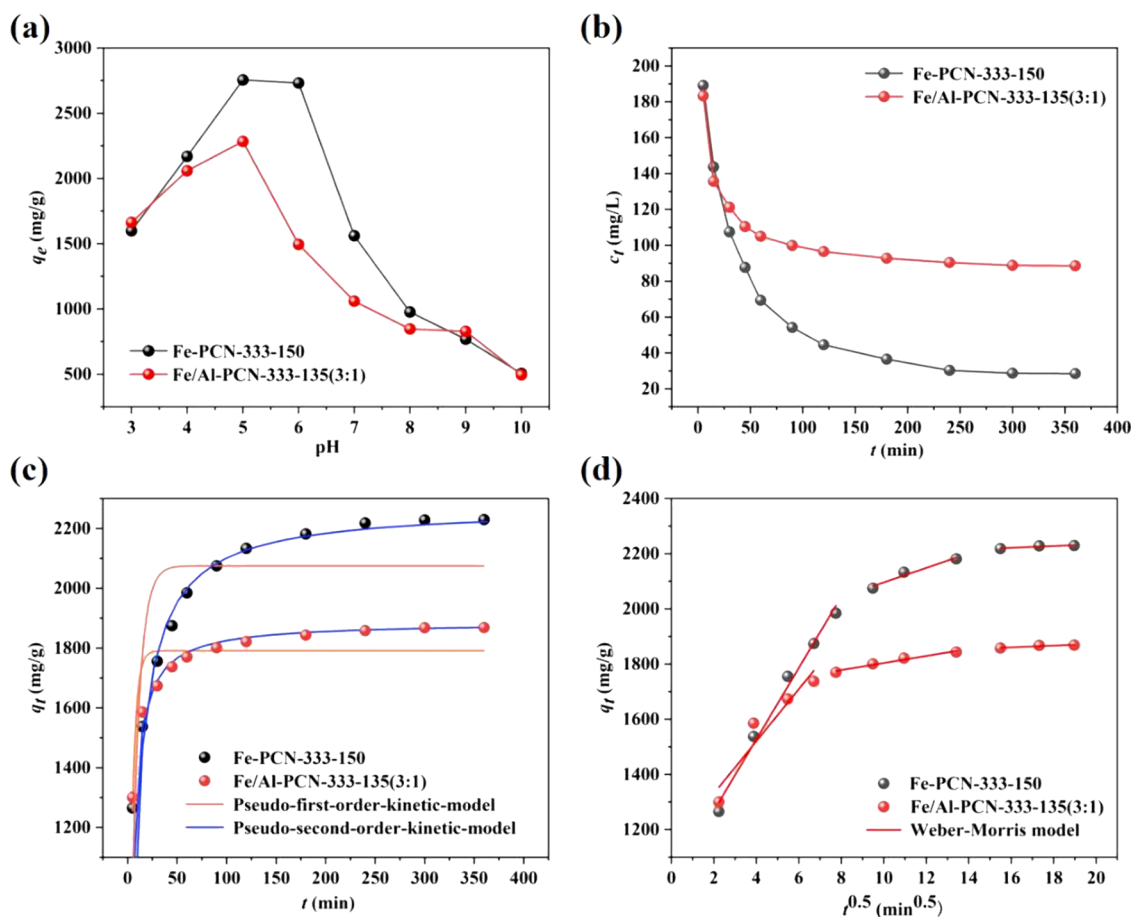


Figure 6. Effect of Fe/Al-PCN-333–135(3:1) and Fe-PCN-333–150 on the CR adsorption capacity at different (a) initial pH values and (b) contact times. (c) Adsorption kinetic curves of CR on Fe/Al-PCN-333–135(3:1) and Fe-PCN-333–150 fitted by pseudo-first-order and pseudo-second-order kinetic models. (d) Weber-Morris intraparticle diffusion model for CR adsorption on Fe/Al-PCN-333–135(3:1) and Fe-PCN-333–150, indicating three stages.

order and pseudo-second-order kinetic models for CR adsorption by Fe/Al-PCN-333–135(3:1) and Fe-PCN-333–150 are shown in Figure S5, and the relevant kinetic parameters are listed in Table S4. Their pseudo-second-order models fit better than their pseudo-first-order models, and the correlation coefficient (R^2) is also higher. In addition, the fitted adsorption capacities using the pseudo-second-order model are closer to the experimental adsorption capacities, indicating that the pseudo-second-order model is more accurate in analyzing the CR adsorption behavior by Fe/Al-PCN-333–135(3:1) and Fe-PCN-333–150 (Figure 6c). This result indicates that chemical adsorption plays a major role in the CR adsorption process.

The diffusion mechanism of CR on Fe/Al-PCN-333–135(3:1) and Fe-PCN-333–150 was analyzed using the Weber-Morris intraparticle diffusion model. As can be seen from Figure 6d, the adsorption process can be roughly divided into three stages: surface diffusion, mesopore diffusion, and micropore diffusion. As shown in Table S3, the diffusion constants of Fe/Al-PCN-333–135(3:1) and Fe-PCN-333–150 show a trend of $k_{id,1} > k_{id,2} > k_{id,3}$. For the solid–liquid adsorption process, surface diffusion is very fast and can usually be ignored. The diffusion constants of $k_{id,1}$, $k_{id,2}$, and $k_{id,3}$ correspond to mesoporous diffusion, microporous diffusion, and chemical equilibrium, respectively. The appearance of a

lower diffusion constant of $k_{id,2}$ indicated that the micropore diffusion is the rate-limiting step in the adsorption process.⁴³

3.2.5. Adsorption Isotherms. Figure 7a,b shows the effect of the initial concentration of CR on the adsorption capacities of Fe/Al-PCN-333–135(3:1) and Fe-PCN-333–150. As the initial CR concentration increases from 100 to 1000 mg/L, the adsorption capacity of Fe/Al-PCN-333–135(3:1) and Fe-PCN-333–150 gradually increased while the removal efficiency gradually decreased. Figure S6 shows the color changes before and after the adsorption of CR by Fe/Al-PCN-333–135(3:1) and Fe-PCN-333–150 at 200 mg/L. Significantly, the removal efficiency of CR by these two materials is very high at low concentrations. To further understand the process of CR adsorbed onto the two BMOFs and estimate the maximum CR adsorption capacity (q_{max}), the isothermal adsorption data were fitted to the Langmuir and Freundlich models, which are represented as follows

$$\text{Langmuir model: } \frac{c_e}{q_e} = \frac{c_e}{q_{max}} + \frac{1}{K_L q_{max}} \quad (9)$$

$$\text{Freundlich model: } \ln q_e = \frac{1}{n} \ln c_e + \ln K_F \quad (10)$$

where q_{max} (mg/g) is the maximum adsorption capacity and K_L and K_F are the adsorption constants for the Langmuir and Freundlich models, respectively.

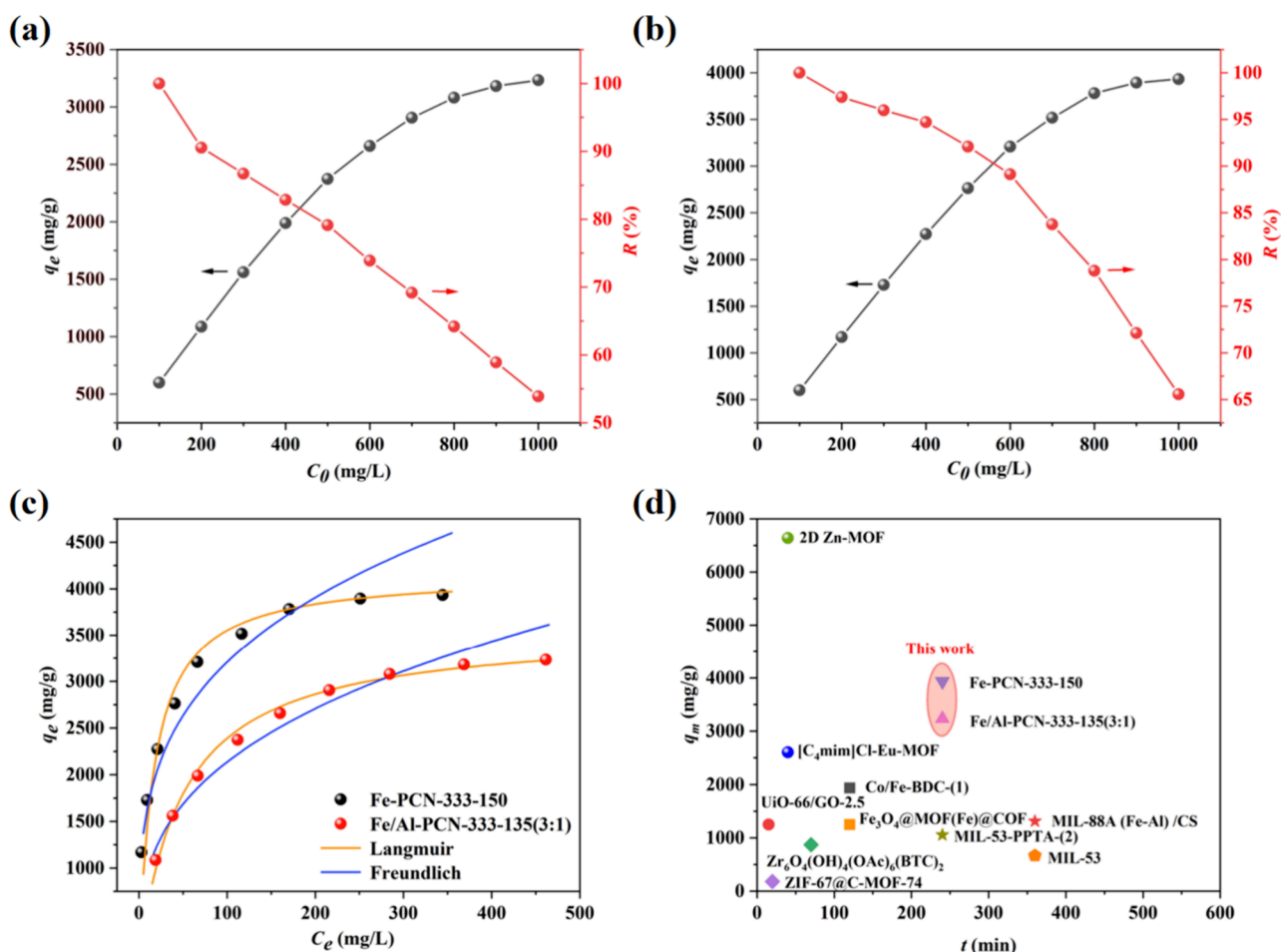


Figure 7. Effect of the initial CR concentration on the adsorption of CR by (a) Fe/Al-PCN-333-135(3:1) and (b) Fe-PCN-333-150. (c) Adsorption isotherm of Fe/Al-PCN-333-135(3:1) and Fe-PCN-333-150 adsorbing CR. (d) Comparison of the q_{max} and equilibrium adsorption times of Fe/Al-PCN-333-135(3:1) and Fe-PCN-333-150 with other reported adsorbents.

Table 1. Comparison of CR Adsorption Capacities of Various Adsorbents

adsorbents	t (min)	T (K)	dosage (mg/mL)	q_{max} (mg/g)	refs
Co/Fe-BDC-(1)	120	298	1	1935.68	44
UiO-66/GO-2.5	15	303	0.01	1250	45
2D Zn-MOF	40	298	0.083	6639.55	46
ZIF-67@C-MOF-74	20	298	1	180	47
Fe ₃ O ₄ @MOF(Fe)@COF	120	318	0.02	1250.02	48
MIL-53-PPTA-(2)	240	298	1	1053.41	49
MIL-53	360	298	1	666.67	49
[C ₄ mim]Cl-Eu-MOF	40	303	0.1	2606	50
MIL-88A (Fe-Al) /CS	360	298	0.5	1312	1
Zr ₆ O ₄ (OH) ₄ (OAc) ₆ (BTC) ₂	70	298	0.2	870	51
Fe/Al-PCN-333-135(3:1)	240	298	0.167	3233.9	this work
Fe-PCN-333-150	240	298	0.167	3933.0	this work

As depicted in Figure 7c, the adsorption isotherm exhibits a type I shape. The linear fitting, corresponding fitting parameters, and fitting theoretical curves for CR adsorption on Fe/Al-PCN-333-135(3:1) and Fe-PCN-333-150 are shown in Figure 7c, Figure S7, and Table S5, respectively. The correlation coefficient of the Langmuir model ($R^2 > 0.99$) is higher than that of the Freundlich model, indicating that the Langmuir model can better describe the adsorption of CR on the two materials. In addition, the theoretical value of q_{max} is basically consistent with the experimental value. As a result, we

concluded that CR is adsorbed on the surface of Fe/Al-PCN-333-135(3:1) and Fe-PCN-333-150 in the monolayer form. The experimental q_{max} values of Fe/Al-PCN-333-135(3:1) and Fe-PCN-333-150 for CR were 3233.9 and 3933.0 mg/g, respectively, which are much higher than that of most materials reported in the literatures (Figure 7d and Table 1). Therefore, Fe/Al-PCN-333-135(3:1) and Fe-PCN-333-150 are very promising materials for the treatment of CR-contaminated wastewater.

Table 2. Thermodynamic Parameters of the CR Adsorption of Fe/Al-PCN-333-135(3:1) and Fe-PCN-333-150 at Different Temperatures

adsorbents	ΔH^0 (kJ/mol)	ΔS^0 (J·mol ⁻¹ ·K ⁻¹)	ΔG^0 (kJ/mol)		
			298 K	308 K	318 K
Fe/Al-PCN-333-135(3:1)	7.048	39.771	-4.804	-5.201	-5.599
Fe-PCN-333-150	13.939	66.948	-6.012	-6.681	-7.350

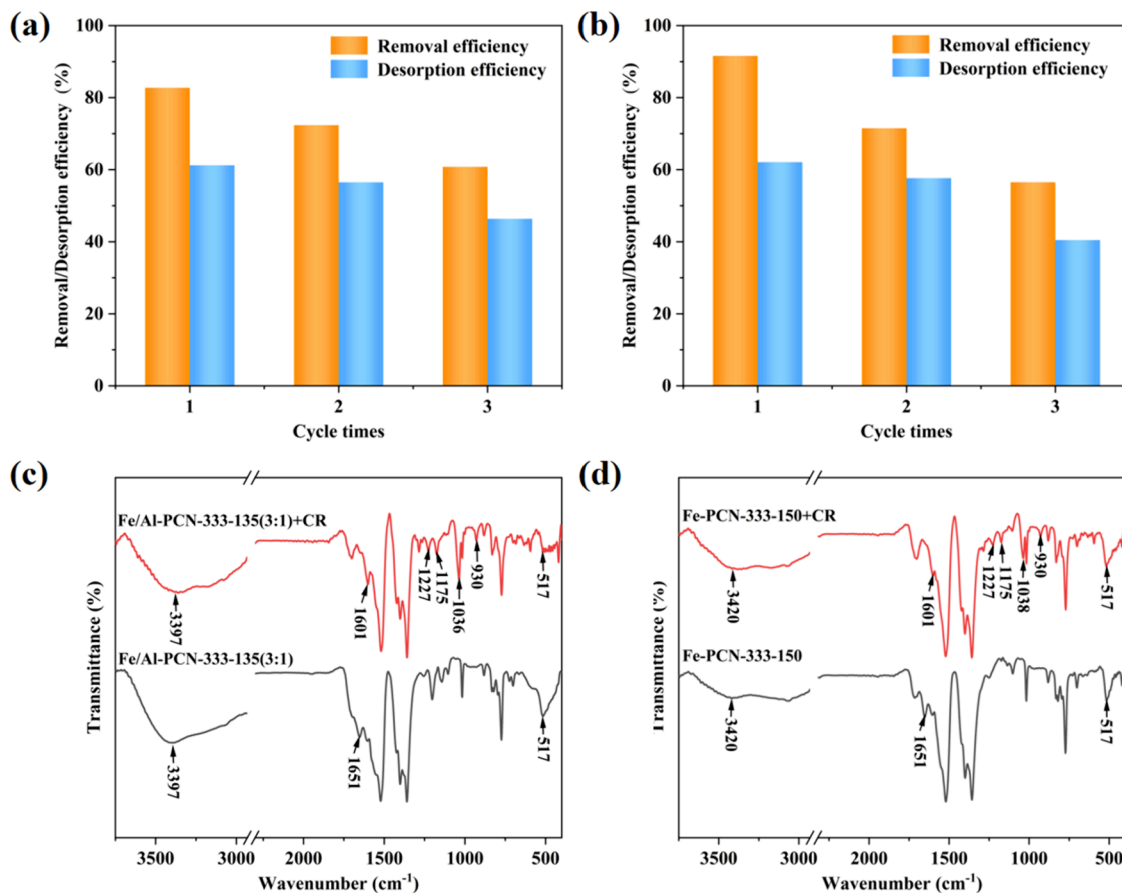


Figure 8. Adsorption–desorption cycle experiments of (a) Fe/Al-PCN-333-135(3:1) and (b) Fe-PCN-333-150. The FT-IR spectra for (c) Fe/Al-PCN-333-135(3:1) and (d) Fe-PCN-333-150 before and after CR adsorption.

3.2.7. Adsorption Thermodynamics. To understand the thermodynamic of the CR adsorption by Fe/Al-PCN-333-135(3:1) and Fe-PCN-333-150 and to evaluate its dependency on temperature, the adsorption capacities of Fe/Al-PCN-333-135(3:1) and Fe-PCN-333-150 were measured at 298, 308, and 318 K. The thermodynamic parameters were calculated as follows:

$$\Delta G^0 = -RT \ln \frac{q_e}{c_e} \quad (11)$$

$$\Delta G^0 = \Delta H^0 - T\Delta S^0 \quad (12)$$

$$\ln \frac{q_e}{c_e} = -\frac{\Delta H^0}{RT} + \frac{\Delta S^0}{R} \quad (13)$$

where ΔS^0 , ΔG^0 , and ΔH^0 represented the change of standard entropy, Gibbs free energy, and enthalpy of the adsorption, respectively. T was the absolute temperature in Kelvin (K), and R was the ideal gas constant (8.314 J·mol⁻¹·K⁻¹).

The CR adsorption capacities of Fe/Al-PCN-333-135(3:1) and Fe-PCN-333-150 at different temperatures are shown in

Figure S8a. As the temperature increases, the adsorption capacities of both materials increases slowly. To evaluate the effect of temperature on the adsorption process, we plotted the $\ln(q_e/c_e)$ values against $1/T$ for the CR adsorption on Fe/Al-PCN-333-135(3:1) and Fe-PCN-333-150, as shown in Figure S8b. A linear regression analysis was performed to determine the thermodynamic parameters, and the results are listed in Table 2. The negative values of ΔG^0 indicate that the adsorption process is thermodynamically favorable and spontaneous at all of the temperatures studied. This suggests that the adsorbent material has a strong affinity for CR, driving the adsorption process. The decrease in ΔG^0 with the temperature indicates that the adsorption process becomes favorable at higher temperatures. Moreover, the positive values of ΔH^0 and ΔS^0 indicate that the CR adsorption on Fe/Al-PCN-333-135(3:1) and Fe-PCN-333-150 is an endothermic process, accompanied by an increase in disorder or randomness of the solid–liquid interface. This may be attributed to the replacement of ordered water molecules on the surface of BMOFs by CR during the adsorption process.

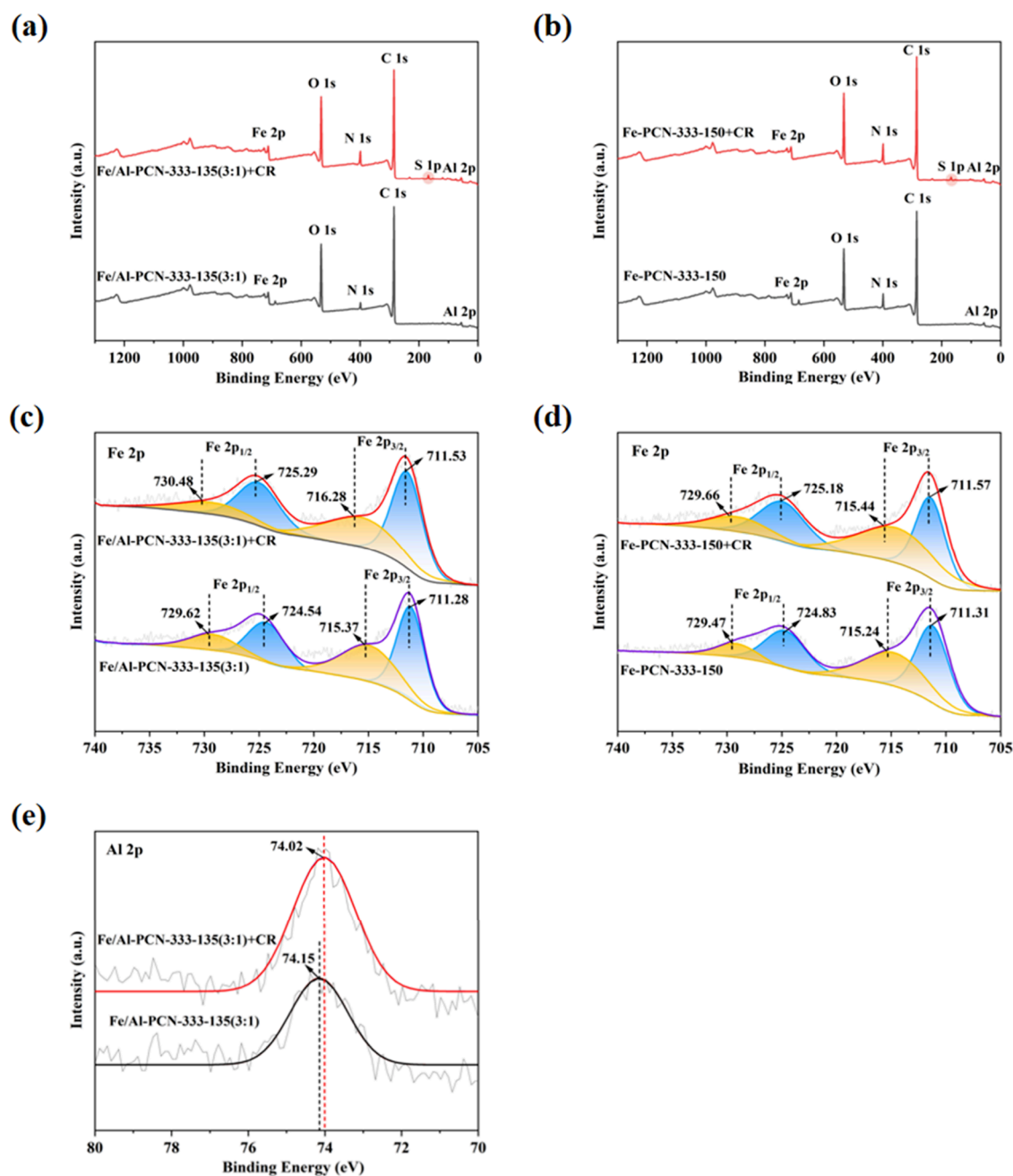


Figure 9. XPS spectra before and after CR adsorption: (a) wide-scan spectra of Fe/Al-PCN-333-135(3:1) and (b) Fe-PCN-333-150; Fe 2p spectra of (c) Fe/Al-PCN-333-135(3:1) and (d) Fe-PCN-333-150 and (e) Al 2p spectra of Fe/Al-PCN-333-135(3:1).

3.3. Adsorbents' Regeneration and Reuse. Adsorbents that can be reused have more advantages in practical applications because the reuse of materials can reduce the cost of adsorption.^{52–54} The regeneration of adsorbents is an important step in reuse, and we used ethanol and acetone as eluents to regenerate Fe/Al-PCN-333-135(3:1) and Fe-PCN-333-150. The advantage of using organic solvent is that it facilitates the recovery of the CR dye through drying the solvent. As depicted in Figures S9 and S10, the desorption efficiency of ethanol is higher than that of acetone. Therefore, we used ethanol as an eluent to carry out the adsorption–desorption cycle experiments. Figure 8a,b shows the adsorption–desorption cycles of CR. It can be observed that, with the increase in the cycle number, the removal efficiency of CR and the desorption efficiency gradually decrease. The CR

removal efficiency of Fe/Al-PCN-333-135(3:1) decreased from 82.7% (the first cycle) to 72.3% (the second cycle) then to 60.8% (the third cycle). The Fe-PCN-333-150 removal efficiency of CR decreased from 91.6% (the first cycle) to 71.5% (the second cycle) then to 56.5% (the third cycle). The decrease of CR removal efficiency is a result of the adsorbed CR being partially retained on the adsorbent, and the adsorption sites cannot be completely regenerated.⁵⁵ After the third cycle, Fe/Al-PCN-333-135(3:1) and Fe-PCN-333-150 still maintained an acceptable adsorption capacity (1458.8 and 1355.8 mg/g, respectively), indicating that the two materials have good reusability.

3.4. Adsorption Mechanism. To further explore the adsorption mechanism of CR by Fe/Al-PCN-333-135(3:1) and Fe-PCN-333-150, FT-IR and XPS spectra were used to

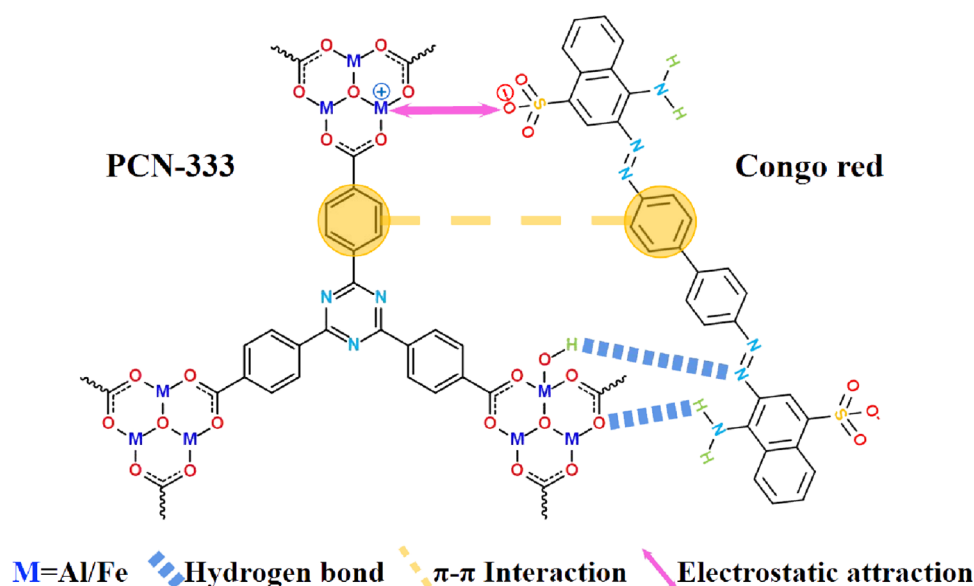


Figure 10. Proposed schematic diagram of the adsorption mechanism for CR adsorbed on PCN-333.

characterize the functional groups, elements, and binding energies of Fe/Al-PCN-333–135(3:1) and Fe-PCN-333–150 before and after CR adsorption. The FT-IR spectra of Fe/Al-PCN-333–135(3:1) and Fe-PCN-333–150 before and after CR adsorption are shown in Figure 8c,d. CR has a stretching vibration of S=O in the $-\text{SO}_3^-$ group at 1222, 1177, and 1060 cm^{-1} , a stretching vibration in the $-\text{N}=\text{N}-$ group at 1584 cm^{-1} , and a characteristic peak at 930 cm^{-1} for the biphenyl group.⁵⁶ After CR adsorption, the peak of Fe/Al-PCN-333–135(3:1) and Fe-PCN-333–150 at 1651 cm^{-1} moved to 1601 cm^{-1} , which was caused by the overlap between the stretching vibration of the carboxyl group in PCN-333 and the stretching vibration of the $-\text{N}=\text{N}-$ group in CR. Moreover, the widening of adsorption peaks at 3420/3397 cm^{-1} is related to the overlap of the absorption peak of N–H and O–H stretching vibrations. These results indicated the π – π interaction and hydrogen bond formation during the adsorption process.^{4,44,45} Furthermore, Fe/Al-PCN-333–135(3:1) and Fe-PCN-333–150 adsorbed by CR appeared with new peaks at 1227, 1175, 1036/1038, and 930 cm^{-1} , and the peak at 517 cm^{-1} was widened. The stretching vibration peak of S=O in the $-\text{SO}_3^-$ group of CR was shifted after adsorption, indicating that there was electrostatic attraction between the metal in PCN-333 and the $-\text{SO}_3^-$ group of CR in the adsorption process.

The XPS spectra of Fe/Al-PCN-333–135(3:1) and Fe-PCN-333–150 before and after CR adsorption are shown in Figure 9a–e. After Fe/Al-PCN-333–135(3:1) and Fe-PCN-333–150 adsorbed the CR, a new peak of S 1p appeared on the wide-scan XPS spectrum (Figure 9a,b). This shows that CR was successfully captured on the surface of Fe/Al-PCN-333–135(3:1) and Fe-PCN-333–150. As depicted in Figure 9c–e, after Fe/Al-PCN-333–135(3:1) and Fe-PCN-333–150 adsorbed CR, the peaks of Fe 2p moved toward higher binding energy and the Al 2p peak showed a slight shift, indicating that both Fe and Al form new chemical bonds. Combined with the above FT-IR analysis, the Fe/Al–O–S bonds between PCN-333 and CR was formed after the materials adsorbed CR.

Based on the above results and analysis, it is proven that Fe/Al-PCN-333–135(3:1) and Fe-PCN-333–150 adsorb CR

through a π – π interaction, hydrogen bond, and electrostatic attraction. The possible schematic diagram of adsorption mechanism is shown in Figure 10.

4. CONCLUSIONS

In this study, Fe/Al PCN-333 μB OFs with different crystal structures and specific surface areas were prepared successfully by a solvothermal method at different temperatures. Among them, Fe-PCN-333–150 and Fe/Al-PCN-333–135(3:1) have a relatively high specific surface area and excellent CR adsorption properties. The adsorption kinetics of the two adsorbents is in accordance with pseudo-second-order kinetics, and the Langmuir model can describe the adsorption of CR on these two materials well. At 298 K, the adsorption capacities of Fe/Al-PCN-333–135(3:1) and Fe-PCN-333–150 for CR were up to 3233.9 and 3933.0 mg/g, respectively. The elevated adsorption capacities of the two adsorbents are ascribed to their high specific surface area and pore volume, engendering ample adsorption sites and facilitating the diffusion of the adsorbed substances. FT-IR and XPS spectral results show that the main mechanism of CR adsorption by Fe/Al-PCN-333–135(3:1) and Fe-PCN-333–150 is a π – π interaction, hydrogen bonds, and electrostatic attraction. This work has shown that Fe/Al-PCN-333–135(3:1) and Fe-PCN-333–150 are effective adsorbents for the treatment of dye wastewater.

■ ASSOCIATED CONTENT

Data Availability Statement

Data will be made available on request.

Supporting Information

The Supporting Information is available free of charge at <https://pubs.acs.org/doi/10.1021/acsomega.3c09256>.

Structural diagram of PCN-333; standard curve of CR; particle size, crystallinity table, and N_2 adsorption–desorption test result table of PCN-333–135 series samples and PCN-333–150 series samples; linear fitting results of Fe/Al-PCN-333–135(3:1) and Fe-PCN-333–150 kinetic models and corresponding table; linear fitting results of Fe/Al-PCN-333–135(3:1) and Fe-

PCN-333–150 adsorption isotherm models and corresponding table; effect of the temperature on the adsorption of CR by Fe-PCN-333–150 and Fe/Al-PCN-333–135(3:1) and the thermodynamic analysis of the relationship between $\ln(q_e/c_e)$ and $1/T$; time course of desorption of CR from Fe/Al-PCN-333–135(3:1) and Fe-PCN-333–150 by different eluents and the color changes before and after CR adsorption by Fe/Al-PCN-333–135(3:1) and Fe-PCN-333–150; and photographs of CR desorbed with ethanol and acetone from Fe/Al-PCN-333–135(3:1) and Fe-PCN-333–150 (PDF)

AUTHOR INFORMATION

Corresponding Authors

Xufeng Zhang – College of Chemistry and Chemical Engineering, Yunnan Normal University, Kunming 650092, China; orcid.org/0000-0002-4384-9317; Phone: +86-13888430046; Email: xzfzhangkm@163.com; Fax: +86-871-65941088

Jing Shen – College of Chemistry and Chemical Engineering, Yunnan Normal University, Kunming 650092, China; Email: shenjing@ynnu.edu.cn

Authors

Boxi Li – College of Chemistry and Chemical Engineering, Yunnan Normal University, Kunming 650092, China

Aihua Zhang – College of Chemistry and Chemical Engineering, Yunnan Normal University, Kunming 650092, China

He Huang – College of Chemistry and Chemical Engineering, Yunnan Normal University, Kunming 650092, China

Complete contact information is available at:

<https://pubs.acs.org/10.1021/acsomega.3c09256>

Author Contributions

B.L. conducted the investigation, methodology, and writing—original draft. J.S. participated in the investigation, writing (review and editing), and funding acquisition. X.Z. contributed in conceptualization, supervision, writing (review and editing), and funding acquisition. A.Z. contributed in result interpretation. H.H. participated in the investigation and methodology.

Notes

The authors declare no competing financial interest.

ACKNOWLEDGMENTS

This work was financially supported by National Natural Science Foundation of China (grant nos. 21965039, 21464017, and 21564018), Natural Science Foundation of Yunnan Province (grant no. 202301AT070071), and Reserve Talents Project for Youth and Middle-Aged Academic and Technical Leaders of Yunnan Province (grant no. 202205AC160032).

REFERENCES

- (1) Zhao, S.; Li, Y.; Wang, M.; Chen, B.; Zhang, Y.; Sun, Y.; Chen, K.; Du, Q.; Wang, Y.; Pi, X.; et al. Efficient adsorption of Congo red by micro/nano MIL-88A (Fe, Al, Fe-Al)/chitosan composite sponge: Preparation, characterization, and adsorption mechanism. *Int. J. Biol. Macromol.* **2023**, *239*, No. 124157.
- (2) Han, L.-J.; Ge, F.-Y.; Sun, G.-H.; Gao, X.-J.; Zheng, H.-G. Effective adsorption of Congo red by a MOF-based magnetic material. *Dalton T.* **2019**, *48* (14), 4650–4656.
- (3) Liu, X.; Liu, B.; Eubank, J. F.; Liu, Y. Highly effective and fast removal of anionic carcinogenic dyes via In_3 -cluster-based cationic metal-organic framework with nitrogen-rich ligand. *Mater. Chem. Front.* **2020**, *4* (1), 182–188.
- (4) Obayomi, K. S.; Lau, S. Y.; Ibrahim, O.; Zhang, J. H.; Meunier, L.; Aniobi, M. M.; Atunwa, B. T.; Pramanik, B. K.; Rahman, M. M. Removal of Congo red dye from aqueous environment by zinc terephthalate metal organic framework decorated on silver nanoparticles-loaded biochar: Mechanistic insights of adsorption. *Micropor. Mesopor. Mater.* **2023**, *355*, No. 112568.
- (5) Zhang, F.; Chen, X.; Wu, F. G.; Ji, Y. F. High adsorption capability and selectivity of ZnO nanoparticles for dye removal. *Colloid Surface A* **2016**, *509*, 474–483.
- (6) Murcia, M. D.; Gómez, M.; Gómez, E.; Gómez, J. L.; Christofi, N. Photodegradation of congo red using XeBr, KrCl and Cl_2 barrier discharge excilamps: A kinetics study. *Desalination* **2011**, *281*, 364–371.
- (7) Ma, C.; Wang, F.; Zhang, C.; Yu, Z.; Wei, J.; Yang, Z.; Li, Y.; Li, Z.; Zhu, M.; Shen, L.; et al. Photocatalytic decomposition of Congo red under visible light irradiation using MgZnCr-TiO_2 layered double hydroxide. *Chemosphere* **2017**, *168*, 80–90.
- (8) Prajapati, K.; Sorokhaibam, L. G.; Bhandari, V. M.; Killedar, D. J.; Ranade, V. V. Differentiating process performance of various coagulants in removal of Congo red and orange G dyes. *Int. J. Chem. React. Eng.* **2016**, *14* (1), 195–211.
- (9) Liu, L.; Yu, L.; Borjigin, B.; Liu, Q.; Hou, D. Fabrication of thin-film composite nanofiltration membranes with improved performance using β -cyclodextrin as monomer for efficient separation of dye/salt mixtures. *Appl. Surf. Sci.* **2021**, *539*, No. 148284.
- (10) Shaban, M.; Ashraf, A. M.; AbdAllah, H.; Abd El-Salam, H. M. Titanium dioxide nanoribbons/multi-walled carbon nanotube nanocomposite blended polyethersulfone membrane for brackish water desalination. *Desalination* **2018**, *444*, 129–141.
- (11) Mohammadikish, M.; Ghaderi, A.; Kazemi-Andalib, F. Selective anionic dye adsorption by a new water-tolerant nickel-based coordination polymer. *J. Mater. Sci.* **2020**, *55* (29), 14656–14663.
- (12) Zhao, Y.; Zhao, Y.; Guo, Z.; Zhou, D.; Yuan, S.; Zhang, X.; Chu, H. Cd^{2+} and Zn^{2+} complexes with 2,4,6-tri(2-pyridyl)-s-triazine and terephthalate for rapid, high-capacity adsorption of Congo red. *ChemistryOpen* **2023**, *12* (2), e202200176.
- (13) Kyzas, G. Z.; Deliyanni, E. A.; Lazaridis, N. K. Magnetic modification of microporous carbon for dye adsorption. *J. Colloid Interface Sci.* **2014**, *430*, 166–173.
- (14) Feng, C.; Ren, P.; Huo, M.; Dai, Z.; Liang, D.; Jin, Y.; Ren, F. Facile synthesis of trimethylammonium grafted cellulose foams with high capacity for selective adsorption of anionic dyes from water. *Carbohydr. Polym.* **2020**, *241*, No. 116369.
- (15) Costa-Marrero, Y.; de Andrade, M. B.; Ellena, J.; Duque-Rodríguez, J.; Fariás, T.; Autié-Castro, G. Zeolite/ZnO composites based on a Cuban natural clinoptilolite and preliminary evaluation in methylene blue adsorption. *Mater. Res. Express* **2020**, *7* (1), No. 015066.
- (16) Aly, R. O. Implementation of chitosan inductively modified by γ -rays copolymerization with acrylamide in the decontamination of aqueous basic dye solution. *Arab. J. Chem.* **2017**, *10* (S1), S121–S126.
- (17) Xiang, C.; Guo, R. H.; Lan, J. W.; Jiang, S. X.; Wang, C.; Du, Z. F.; Cheng, C. Self-assembling porous 3D titanium dioxide-reduced graphene oxide aerogel for the tunable absorption of oleic acid and RhodamineB dye. *J. Alloy. Compd.* **2018**, *735*, 246–252.
- (18) Xu, Y.; Jin, J.; Li, X.; Han, Y.; Meng, H.; Song, C.; Zhang, X. Magnetization of a Cu(II)-1,3,5-benzenetricarboxylate metal-organic framework for efficient solid-phase extraction of Congo Red. *Microchim. Acta* **2015**, *182* (13–14), 2313–2320.
- (19) Wang, F.; Hu, W.; Zhang, S.; Zhu, C.; Fan, Y.; Wang, Q. Ionic liquid-water interfacial synthesis of ionic liquid incorporated metal-organic frameworks with enhanced adsorption properties. *Micropor. Mesopor. Mater.* **2023**, *351*, No. 112480.
- (20) Valadi, F. M.; Ekramipooya, A.; Gholami, M. R. Selective separation of Congo Red from a mixture of anionic and cationic dyes using magnetic-MOF: Experimental and DFT study. *J. Mol. Liq.* **2020**, *318*, No. 114051.

- (21) Karmakar, S.; Dechnik, J.; Janiak, C.; De, S. Aluminium fumarate metal-organic framework: A super adsorbent for fluoride from water. *J. Hazard. Mater.* **2016**, *303*, 10–20.
- (22) Prasetya, N.; Li, K. Synthesis of defective MOF-801 via an environmentally benign approach for diclofenac removal from water streams. *Sep. Purif. Technol.* **2022**, *301*, No. 122024.
- (23) Ji, C.; Ren, Y.; Yu, H.; Hua, M.; Lv, L.; Zhang, W. Highly efficient and selective Hg(II) removal from water by thiol-functionalized MOF-808: Kinetic and mechanism study. *Chem. Eng. J.* **2022**, *430*, No. 132960.
- (24) Guo, X.; Kong, L.; Ruan, Y.; Diao, Z.; Shih, K.; Su, M.; Hou, L. a.; Chen, D. Green and facile synthesis of cobalt-based metal-organic frameworks for the efficient removal of Congo red from aqueous solution. *J. Colloid Interface Sci.* **2020**, *578*, 500–509.
- (25) Furukawa, H.; Gándara, F.; Zhang, Y.-B.; Jiang, J.; Queen, W. L.; Hudson, M. R.; Yaghi, O. M. Water adsorption in porous metal-organic frameworks and related materials. *J. Am. Chem. Soc.* **2014**, *136* (11), 4369–4381.
- (26) Zhang, W.; Zhang, R. Z.; Huang, Y. Q.; Yang, J. M. Effect of the synergetic interplay between the electrostatic interactions, size of the dye molecules, and adsorption sites of MIL-101(Cr) on the adsorption of organic dyes from aqueous solutions. *Cryst. Growth Des.* **2018**, *18* (12), 7533–7540.
- (27) Zhang, A. B.; Liu, B. Y.; Liu, M. X.; Xie, Z. Y.; Wang, D.; Feng, G. N. The adsorption properties of defect controlled metal-organic frameworks of UiO-66. *Sep. Purif. Technol.* **2021**, *270*, No. 118842.
- (28) Lan, X.; Huang, N.; Wang, J.; Wang, T. A general and facile strategy for precisely controlling the crystal size of monodispersed metal-organic frameworks via separating the nucleation and growth. *Chem. Commun.* **2018**, *54* (6), 584–587.
- (29) Becker, T. M.; Heinen, J.; Dubbeldam, D.; Lin, L.-C.; Vlugt, T. J. H. Polarizable force fields for CO₂ and CH₄ adsorption in M-MOF-74. *J. Phys. Chem. C* **2017**, *121* (8), 4659–4673.
- (30) Yang, H.; Hu, S.; Zhao, H.; Luo, X.; Liu, Y.; Deng, C.; Yu, Y.; Hu, T.; Shan, S.; Zhi, Y.; et al. High-performance Fe-doped ZIF-8 adsorbent for capturing tetracycline from aqueous solution. *J. Hazard. Mater.* **2021**, *416*, No. 126046.
- (31) Liu, Q.; Yang, J.-M.; Jin, L.-N.; Sun, W.-Y. Metal ion induced porous HKUST-1 nano/microcrystals with controllable morphology and size. *CrystEngComm* **2016**, *18* (22), 4127–4132.
- (32) Gu, Y.; Xie, D. H.; Wang, Y. C.; Qin, W. X.; Zhang, H. M.; Wang, G. Z.; Zhang, Y. X.; Zhao, H. J. Facile fabrication of composition-tunable Fe/Mg bimetal-organic frameworks for exceptional arsenate removal. *Chem. Eng. J.* **2019**, *357*, 579–588.
- (33) Shen, W.; Guo, X.; Pang, H. Effect of Solvothermal Temperature on Morphology and Supercapacitor Performance of Ni-MOF. *Molecules* **2022**, *27* (23), 8226.
- (34) Jiang, H.; Wang, Q.; Wang, H.; Chen, Y.; Zhang, M. Temperature effect on the morphology and catalytic performance of Co-MOF-74 in low-temperature NH₃-SCR process. *Catal. Commun.* **2016**, *80*, 24–27.
- (35) Park, J.; Feng, D.; Zhou, H.-C. Structure-assisted functional anchor implantation in robust metal-organic frameworks with ultralarge pores. *J. Am. Chem. Soc.* **2015**, *137* (4), 1663–1672.
- (36) Feng, D.; Liu, T. F.; Su, J.; Bosch, M.; Wei, Z.; Wan, W.; Yuan, D.; Chen, Y. P.; Wang, X.; Wang, K.; et al. Stable metal-organic frameworks containing single-molecule traps for enzyme encapsulation. *Nat. Commun.* **2015**, *6* (1), 5979.
- (37) Marri, S. R.; Chauhan, N.; Tiwari, R. K.; Kumar, J.; Behera, J. N. Two novel 3D-MOFs (Ca-TATB and Co-HKUST): Synthesis, structure and characterization. *Inorg. Chim. Acta* **2018**, *478*, 8–14.
- (38) Zhang, X. X.; Bao, T.; Wei, F.; Wang, S. C. Zeotype porous coordination networks as potential adsorbents for removing non-steroidal anti-inflammatory drugs from water. *Colloid Surface A* **2022**, *640*, No. 128401.
- (39) Tao, Y.; Yang, B.; Wang, F.; Yan, Y.; Hong, X.; Xu, H.; Xia, M.; Wang, F. Green synthesis of MOF-808 with modulation of particle sizes and defects for efficient phosphate sequestration. *Sep. Purif. Technol.* **2022**, *300*, No. 121825.
- (40) Aboubakr, A. E. A.; Roubay, W. M. A. E.; Khan, M. D.; Farghali, A. A.; Revaprasadu, N. ZnCr-CO₃ LDH/ruptured tubular g-C₃N₄ composite with increased specific surface area for enhanced photoelectrochemical water splitting. *Appl. Surf. Sci.* **2020**, *508*, No. 145100.
- (41) Hashjin, M. A.; Zarshad, S.; Emrooz, H. B. M.; Sadeghzadeh, S. Enhanced atmospheric water harvesting efficiency through green-synthesized MOF-801: a comparative study with solvothermal synthesis. *Sci. Rep.* **2023**, *13*, 16983.
- (42) Xu, R.; Ji, Q.; Zhao, P.; Jian, M.; Xiang, C.; Hu, C.; Zhang, G.; Tang, C.; Liu, R.; Zhang, X.; et al. Hierarchically porous UiO-66 with tunable mesopores and oxygen vacancies for enhanced arsenic removal. *J. Mater. Chem. A* **2020**, *8* (16), 7870–7879.
- (43) Wang, J.; Guo, X. Adsorption kinetics and isotherm models of heavy metals by various adsorbents: An overview. *Crit. Rev. Env. Sci. Tec.* **2023**, *53* (21), 1837–1865.
- (44) Liu, Y.; Qiu, G. Y.; Liu, Y. F.; Niu, Y. Z.; Qu, R. J.; Ji, C. N.; Wang, Y.; Zhang, Y.; Sun, C. M. Fabrication of CoFe-MOF materials by different methods and adsorption properties for Congo red. *J. Mol. Liq.* **2022**, *360*, No. 119405.
- (45) Mukherjee, D.; Das, P.; Prasad, G. N.; Katha, A. R.; Gumma, S.; Mandal, B. Hierarchical graphite oxide decorated UiO-66 for ultrahigh adsorption of dye with synergistic effect of ultrasonication: Experimental and density functional theory study. *Sep. Purif. Technol.* **2022**, *294*, No. 121217.
- (46) Liu, L.-L.; Chen, J.; Zhang, Y.; Yu, C.-X.; Du, W.; Sun, X.-Q.; Zhang, J.-L.; Hu, F.-L.; Mi, Y.; Ma, L.-F. Fabrication of ultrathin single-layer 2D metal-organic framework nanosheets with excellent adsorption performance via a facile exfoliation approach. *J. Mater. Chem. A* **2021**, *9* (1), 546–555.
- (47) del Rio, M.; Turnes Palomino, G.; Palomino Cabello, C. Metal-organic framework@carbon hybrid magnetic material as an efficient adsorbent for pollutant extraction. *ACS Appl. Mater. Interfaces* **2020**, *12* (5), 6419–6425.
- (48) Wang, Q.; Zhao, Y.; Shi, Z.; Sun, X.; Bu, T.; Zhang, C.; Mao, Z.; Li, X.; Wang, L. Magnetic amino-functionalized-MOF (M = Fe, Ti, Zr)@COFs with superior biocompatibility: Performance and mechanism on adsorption of azo dyes in soft drinks. *Chem. Eng. J.* **2021**, *420*, No. 129955.
- (49) Liu, Y.; Qiu, G.; Li, T.; Yan, A.; Liu, Y.; Qu, R.; Sun, C. Preparation of metal organic framework hybridizing with poly(p-phenylene terephthalamide) fiber and adsorption properties for anionic dye. *Pigm. Resin Technol.* **2023**, *52* (1), 60–72.
- (50) Xiao, Y.; Chen, F.; Zhu, X.; Qin, H.; Huang, H.; Zhang, Y.; Yin, D.; He, X.; Wang, K. Ionic liquid-assisted formation of lanthanide metal-organic framework nano/microrods for superefficient removal of Congo red. *Chem. Res. Chinese U.* **2015**, *31* (6), 899–903.
- (51) Farhadi, S.; Manteghi, F.; Tondfekar, R. Removal of Congo red by two new zirconium metal-organic frameworks: kinetics and isotherm study. *Monatsh. Chem.* **2019**, *150* (2), 193–205.
- (52) Akram, M.; Xu, X.; Gao, B.; Wang, S.; Khan, R.; Yue, Q.; Duan, P.; Dan, H.; Pan, J. Highly efficient removal of phosphate from aqueous media by pomegranate peel co-doping with ferric chloride and lanthanum hydroxide nanoparticles. *J. Clean. Prod.* **2021**, *292*, No. 125311.
- (53) Bhatti, H. N.; Safa, Y.; Yakout, S. M.; Shair, O. H.; Iqbal, M.; Nazir, A. Efficient removal of dyes using carboxymethyl cellulose/alginate/polyvinyl alcohol/rice husk composite: Adsorption/desorption, kinetics and recycling studies. *Int. J. Biol. Macromol.* **2020**, *150*, 861–870.
- (54) Mirzaei, K.; Jafarpour, E.; Shojaei, A.; Khasraghi, S. S.; Jafarpour, P. An investigation on the influence of highly acidic media on the microstructural stability and dye adsorption performance of UiO-66. *Appl. Surf. Sci.* **2023**, *618*, No. 156531.
- (55) Yin, T.; Zhang, X.; Shao, S.; Xiang, T.; Zhou, S. Covalently crosslinked sodium alginate/poly(sodium p-styrenesulfonate) cryogels for selective removal of methylene blue. *Carbohydr. Polym.* **2023**, *301*, No. 120356.

(56) Khan, A. A.; Molla, A.; Chowdhury, A.; Kumari, S.; Hussain, S. Surface-charge-controlled synthesis of ZnIn₂S₄ nanosheet-based materials for selective adsorption of organic dyes. *ACS Appl. Nano Mater.* **2021**, *4* (4), 4114–4128.